Remote Sensing of Environment 136 (2013) 76–88

Contents lists available at SciVerse ScienceDirect

Remote Sensing of Environment

journal homepage: www.elsevier.com/locate/rse

# Multiple Endmember Spectral Mixture Analysis (MESMA) to map burn severity levels from Landsat images in Mediterranean countries

Carmen Quintano [a,*], Alfonso Fernández-Manso [b], Dar A. Roberts [c]

[a] Electronic Technology Department, University of Valladolid, C/Francisco Mendizábal, s/n, 47014 Valladolid, Spain
[b] Agrarian Science and Engineering Department, University of León, Av. Astorga s/n, 24400 Ponferrada, Spain
[c] Department of Geography, University of California, Santa Barbara, CA 93106, USA

ARTICLE INFO

*Article history:*
Received 13 October 2012
Received in revised form 26 April 2013
Accepted 27 April 2013
Available online xxxx

*Keywords:*
SMA
MESMA
Landsat
Mediterranean countries
Burn severity

ABSTRACT

Forest fires are a major hazard in Mediterranean countries, with an average of 45,000 fires per year. Discrimination of different degrees of burn severity is critical to improve management of fire-affected areas. In this work, an unmixing-based methodology was evaluated in three Mediterranean study areas to estimate burn severity from medium spatial resolution optical satellite data. Post-fire Landsat 5 Thematic Mapper (TM) images were unmixed into four fraction images: non-photosynthetic vegetation and ash (NPV–Ash), green vegetation (GV), soil and shade using Multiple Endmember Spectral Mixture Analysis (MESMA). MESMA decomposes each pixel using different combinations of potential endmembers, overcoming the Linear Spectral Mixture Analysis limitation of using the same number of endmembers to model all image pixels. Next, a decision tree was used to classify the shade normalized fraction images into four classes: unburned and low, moderate, and high levels of burn severity. Finally, the burn severity estimates were validated using error matrix, producer and user accuracies per class, and κ statistic. For reference data, we used 50 plots per class defined from a 50 cm post-fire orthophotography (proportion of dead tree < 50%, low severity; proportion of dead tree between 50 and 90%, moderate severity; and proportion of dead tree > 90%, high severity). MESMA-based burn severity estimates showed a high accuracy (0.80, 0.80, and 0.78) for the three test sites. We conclude that the proposed MESMA based methodology is valid to accurately map burn severity in Mediterranean countries from moderate resolution satellite data.



## 1. Introduction

Worldwide fires affect millions of hectares annually from tropical to boreal regions, removing partially or completely the vegetation layer and affecting the post-fire vegetation composition (Calvo et al., 2008; Epting & Verbyla, 2005; Riaño et al., 2007). In Mediterranean countries, fires are considered a major cause of land degradation with about 0.5 million hectares affected each year by around 45,000 forest fires (Schmuck et al., 2010). Discrimination of different degrees of burn severity is critical to improve management of fire-affected areas, either to help natural regrowth, reduce soil erosion and degradation, or improve landscape diversity (Key, 2005; Lentile et al., 2006). According to Key and Benson (2006), in a broad sense, the consequences of fire in a particular area are governed by short- and long-term processes, so overall severity is an amalgamation of factors. Short-term severity reflects changes to pre-fire community components extending until approximately one year following the fire. Long-term severity reflects unique site conditions that prevail up to ten years into the future in addition to short-term severity. Although the terms fire and burn severity are often used interchangeably (Veraverbeke et al., 2010b), the distinction between them has become the subject of some discussion (Keeley, 2009). Several papers (Bodi et al., 2011; De Santis & Chuvieco, 2007, 2009; De Santis et al., 2009, 2010; Robichaud, 2005) have clarified the use of fire severity to refer to fire behavior conditions, and burn severity to what is left after fire, including short and long-term effects, as proposed by Jain et al. (2004). Following this definition, we established three levels of vegetation burn severity by observing the percentage of green vegetation. As suggested by Hudak et al. (2004), burned sites with predominantly green crowns were classified as low, with predominantly brown crowns as medium, and with predominantly black crowns as high.

Remotely sensed data constitute the method of choice when estimates of fire/burn severity are needed over large areas because of the prohibitive costs and the time needed to conduct fieldwork. The potential of satellite imagery as an alternative for extensive field sampling to quantify both fire and burn severity over large areas has been shown in a large number of studies (e.g. French et al., 2008; Miller & Yool, 2002; Verbyla & Lord, 2008). Many of these studies have used spectral indices for assessing burn severity (e.g. Hudak et al., 2007; Miller & Thode, 2007; Veraverbeke et al., 2011) or for burned area mapping (Quintano

* Corresponding author. Tel.: +34 983186487; fax: +34 983423490.
*E-mail address:* menchu@tele.uva.es (C. Quintano).

0034-4257/$ – see front matter © 2013 Elsevier Inc. All rights reserved.
http://dx.doi.org/10.1016/j.rse.2013.04.017

& Cuesta, 2010; Quintano et al., 2011; Smith et al., 2007b). Normalized Burn Ratio (NBR) and more specifically the differenced Normalized Burn Ratio (dNBR), has become accepted as the standard spectral index to estimate burn severity (e.g. Chen et al., 2011; Epting et al., 2005; French et al., 2008; Key & Benson, 2006; López-García & Caselles, 1991; Soverel et al., 2010; van Wagtendonk et al., 2004; Veraverbeke et al., 2010a). However, as several authors have stated (e.g. De Santis & Chuvieco, 2007; De Santis et al., 2009; Lentille et al., 2009; Roy et al., 2006), methods based on dNBR and other similar spectral indices have limitations: spectral bands used to calculate NBR are not optimal to evaluate the degree of burning, dNBR cannot be optimal for characterizing both burned area and post-fire effects related to severity, among others (see Lentille et al., 2009 for examining the limitations in detail). Other approaches to retrieve burn severity from satellite imagery have been proposed. Some of them are based on radiative transfer models, which provide a more physical basis to estimate this variable (Chuvieco et al., 2007; De Santis & Chuvieco, 2007, 2009; De Santis et al., 2009, 2010). Recent research has highlighted subpixel-based methods as one such alternative (Hudak et al., 2007; Lentile et al., 2006, 2009; Smith et al., 2007a).

The short-term post-fire environment typically consists of a mixture of vegetation and substrate and ash. Thus, monitoring post-fire effects essentially poses a sub-pixel problem at the resolution of most operational satellite systems such as Landsat. Different image analysis techniques to solve the mixing problem exist (e.g. Atkinson et al., 1997; Kokaly et al., 2007) but linear spectral mixture analysis (LSMA) is the most widely technique used (e.g. Riaño et al., 2002; Vila & Barbosa, 2010). LSMA assumes that the reflectance of each mixed pixel is a linear combination of spectra of distinct components or endmembers with the weights representing the abundances of endmembers resident in a mixed pixel (Roberts et al., 1993; Shimabukuro & Smith, 1991). The aim of LSMA is to decompose a mixed pixel into a set of endmember spectra and estimate the proportion of endmembers present in that pixel (fraction images). Fractional abundance can be estimated using a variety of approaches, including least squares (Shimabukuro & Smith, 1991), modified Gramm–Schmidt orthogonal decomposition (Adams et al., 1993) or singular value decomposition (Boardman et al., 1995) as three common approaches. Model fit is often assessed based on the root mean square error (RMSE) error metric.

LSMA, predominately used to map burned area, can surpass the results obtained with more traditional techniques like vegetation indices (Hudak et al., 2007; Quintano et al., 2006; Smith et al., 2007a; Vila & Barbosa, 2010). Furthermore, as Lentile et al. (2006, 2009) pointed out, it also enables estimation of fractional cover components with each multispectral image pixel, including unburned vegetation, soils and charred of fully combusted vegetation, that are directly analogous to traditional 'field severity' assessment of % green, % brown and % black.

Accuracy of LSMA results, however, mainly depends on the endmembers selected. The number of endmembers must account for the number of classes in the pixel, and their spectral separability should be sufficient in order to avoid confusion (Theseira et al., 2002). LSMA is restricted to models in which only one spectrum was allowed for each endmember. For that reason, this model does not incorporate the natural variability in scene conditions (the same material could have different spectral responses). Multiple Endmember SMA (MESMA), presented by Roberts et al. (1998), is widely used to account for within class spectral variability. In this model, allowing multiple endmembers for each endmember class includes natural variability. In addition, because MESMA decomposes each pixel using different combinations of potential endmembers it overcomes the LSMA limitation of using the same number of endmembers to model all pixels, regardless of whether the ground components represented by the endmembers are present in the pixel. MESMA has been applied in a wide range of fields: plant species mapping (Dennison & Roberts, 2003; Roberts et al., 1998; Youngentob et al., 2011), landform mapping (Ballantine et al., 2005), fire temperature mapping (Dennison et al., 2006; Eckmann et al., 2009), and urban remote sensing (Franke et al., 2009; Powell et al., 2007), among others.

Our study explores the potential of using MESMA fraction images to map burn severity levels in Mediterranean countries — an approach that has not been explored in remote sensing of burn severity. A few burn severity studies have been carried out in the Mediterranean Basin (e.g. De Santis & Chuvieco, 2007; De Santis et al., 2009; Díaz-Delgado et al., 2003; Fernández-Manso et al., 2009; Veraverbeke et al., 2010a); but none of them, to our knowledge, used MESMA-based fraction images to estimate the burn severity levels. Thus, this study is the first use of MESMA in Mediterranean countries to map burn severity levels. We use Landsat 5 Thematic Mapper (TM) data, which is the standard choice when working at moderate resolutions. Post-fire orthophotographs were used as reference to measure the accuracy of MESMA-based estimates (specifically, we computed for error matrix and $\kappa$ statistic). Additional measures of accuracy included producer and user accuracies and overall accuracy.

## 2. Materials

### 2.1. Study area

Three study areas were included in this study: Guadalajara, Ávila, and Tenerife provinces, all of them located in Spain (Fig. 1, Table 1).

Our first study area is located in East Central Spain (province of Guadalajara). The topography is rugged with elevation ranging between 1100 m and 1400 m. Rainfall averages 600–800 mm per year, with maximum precipitation recorded in November–December and minimum precipitation taking place during the summer months. *Pinus pinaster* Ait. is the dominant vegetation, mixed with oak forest of *Quercus faginea* Lam. and *Quercus pyrenaica* Willd. The fire in this area burned about 130 km$^2$. The fire lasted 4 days, ending on 16 July 2005. It was caused by human carelessness and helped by very dry weather conditions including a maximum air temperature of 35 °C, relative humidity of 22%, 30 days since the last rainfall event and wind speeds between 10 and 23 km/h. Eleven firefighters died while suppressing the fire, which had a major impact in the national media (De Santis & Chuvieco, 2007; Spanish Environmental Ministry, 2005).

The second study area is located in Central Spain (province of Ávila), at the base of Central Sierra de Gredos Mountains. This region has irregular topography with elevation ranging from around 500 m in the Tiétar River valley to 2300 m at some of the highest peaks. Average summer temperature in this region is 33 °C whereas average winter temperature drops to 1 °C. The average precipitation in this area is 1200 mm per year, yet during the summer months decreases to around zero. According to the Spanish Forestry Map, *P. pinaster* is the main species, followed by *Pinus sylvestris* L. and *Q. pyrenaica* and *Quercus ilex* L. The fire we analyzed started on 28 July 2009 and lasted three days, burning approximately 420 km$^2$ of forested areas. The exceptionally dry conditions, high temperatures and strong winds helped its spread.

Finally, the third study area is located in the north of Tenerife Island (The Canary Islands). The Canary Island pine, *Pinus canariensis* Chr. Sm. ex DC., is an endemic species of the Canary Islands and forms up to 60% of the forest area of the archipelago. The understory can be dense and is characterized by shrubs or small trees such as *Erica arborea* L., and *Myrica faya* L., all species that are found in the evergreen laurel forest, situated below 1000 m (Otto et al., 2009). Our study area includes the Corona Forestal Natural Park, ranging from 300 to 2700 m elevation (Martín et al., 1995). The area is located over a volcanic surface where vegetation is sparse, especially in high elevation areas. Teide Volcano last erupted in 1909. In 2004 there were an alarm for possible eruption due to the existence of big fumaroles and an increase of the magma level. This area was burned in 1983 and again on 27 July 2007 (i.e. 24 years later), affecting about 170 km$^2$ of mostly pine forest (Canary Island pine). The fire in 2007 spread very fast due to

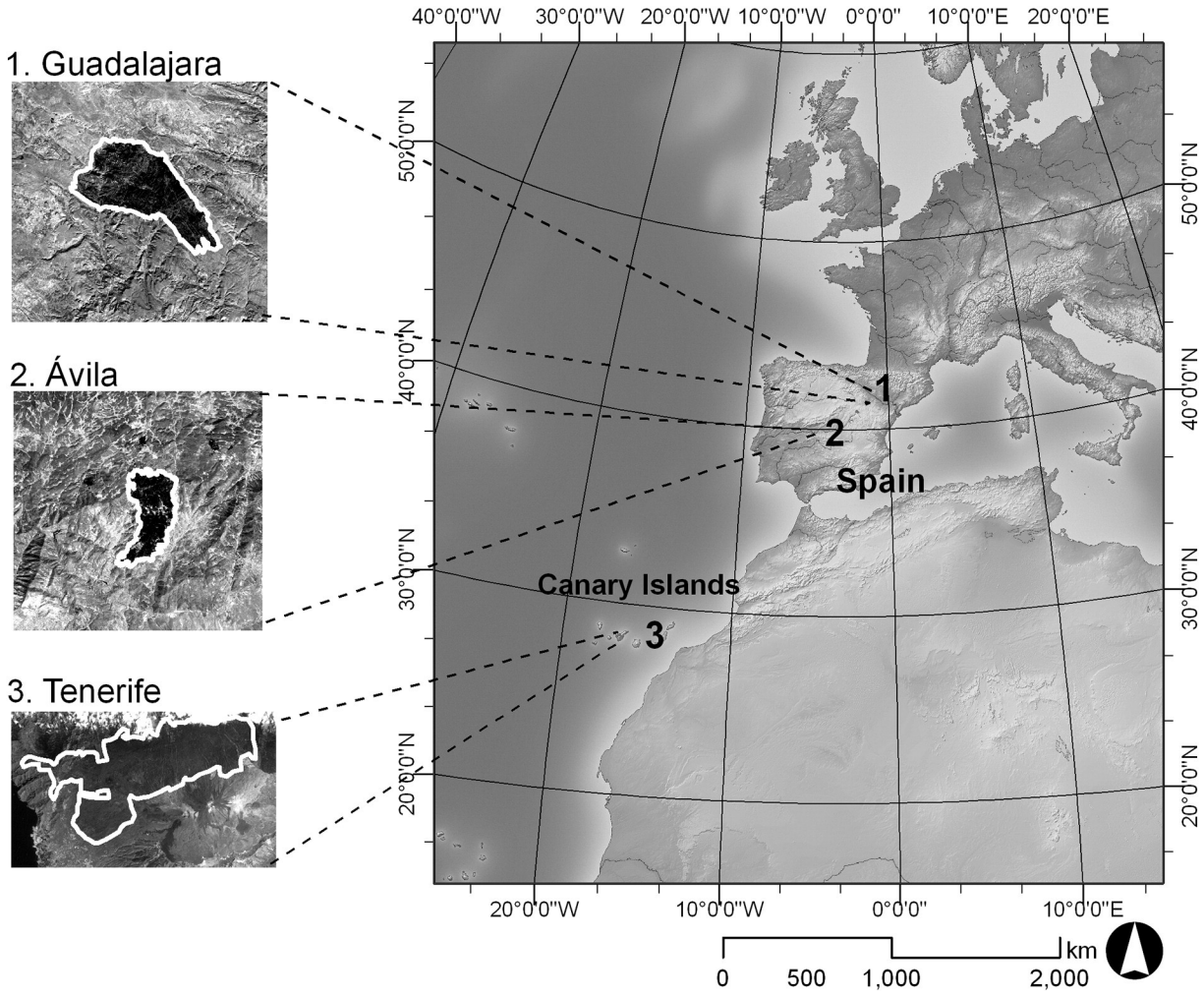


**Fig. 1.** Study areas location.

exceptionally high air temperatures (>40 °C), very low relative humidity (<20%) and strong eastern winds from Africa.

### 2.2. Datasets

In both the Ávila and Tenerife study areas, pre-fire and post-fire Landsat 5 TM images without clouds were located and downloaded from the U.S. Geological Survey (USGS) site (http://glovis.usgs.gov/). All of the images had level L1G processing (systematic correction), providing systematic radiometric and geometric accuracy, scene rotation and georeferencing to a Universal Transverse Mercator (UTM) map projection. In the Guadalajara study area, however, pre-fire and post-fire Landsat 5 TM images were downloaded from the Spanish Remote Sensing National Planning frame (PNT). These images were also radiometrically and geometrically corrected and re-projected to UTM map projection. Table 1 also summarizes the relevant information about the Landsat 5 TM images selected to estimate the burn severity level in each study area.

To validate estimated burn severity levels we used post-fire 50 cm digital orthophotographs provided by the Spanish National Center of Geographic Information (CNIG; http://www.cnig.es/) through the Spanish Aerial Ortho-photography National Planning (PNOA) agency. Specifically, we used a 2006 false-color orthophotograph in the Guadalajara study area, and a 2009 false-color orthophotograph in

**Table 1**
Summary of the characteristics of the study areas and the dataset.

| Study areas | | Guadalajara | Ávila | Tenerife |
|---|---|---|---|---|
| Forest fire | Year | 2005 | 2009 | 2007 |
| | Date | 16 July–2 Aug. | 28–30 July | 27 July–1 Aug. |
| | Affected area ($km^2$) | 128.87 | 42.12 | 171.84 |
| | Forested affected area ($km^2$) | 103.53 | 42.12 | 131.27 |
| Characteristics | Main vegetation | *Pinus pinaster* Ait. | *P. pinaster* Ait. | *Pinus canariensis* Chr. Sm. ex DC |
| | Soil-geology | Red sandstone | Schists and quartzite | Basalt |
| Landsat 5 TM images | Spatial agency[1] | PNT | USGS | USGS |
| | Path/row | 200/32 | 202/32 | 207/40 |
| | Pre-fire image date | 26 June 2005 | 13 July 2009 | 16 January 2007 |
| | Post-fire image date | 14 Sept. 2005 | 30 August 2009 | 28 August 2007 |

[1] PNT: Spanish Remote Sensing National Planning; USGS: U.S. Geological Survey; TM: Thematic Mapper.

the Ávila study area. Orthophotographs were not available in the Tenerife study area. For this reason, we used a post-fire Earth Observation Satellite (Satellite Pour L'observation de la Terre, SPOT) 5 image acquired on 4 August 2007 (immediately post-fire) (2.5 m panchromatic band) and considered as a help-reference the estimates of severity levels obtained by the German Aerospatiale Center (Deutsches Zentrum für Luft- und Raumfahrt, DLR). The official Global Positioning System (GPS) burned area perimeters provided by the respective Spanish Regional Governments were used as well.

As ancillary data, we needed a digital elevation model (DEM) and used the Advanced Spaceborne Thermal Emission and Reflection Radiometer (ASTER) Global Digital Elevation Model Version 2 (GDEM V2) provided by USGS. An Airborne Visible/Infrared Imaging Spectrometer (AVIRIS) image of Santa Barbara, California, acquired on 26 August, 2009 following the May 2009 Jesusita fire, was used as a source of plant canopy, ash and soil spectra. This image was used mainly as a resource for non-photosynthetic vegetation and ash spectra. Additional spectra of vegetation canopies were derived from a spectral library based on a 2007 3.5 m spatial resolution image of the U.C. Santa Barbara campus, including spectra for shrub and herb species and impervious surfaces. All AVIRIS spectra were extracted from reflectance images atmospherically corrected using Modtran radiative transfer code and a ground reference target (see Herold et al., 2004; Roberts et al., 2012).

## 3. Methods

The method proposed in this study comprises the following steps (Fig. 2): pre-processing, the MESMA procedure, classification and

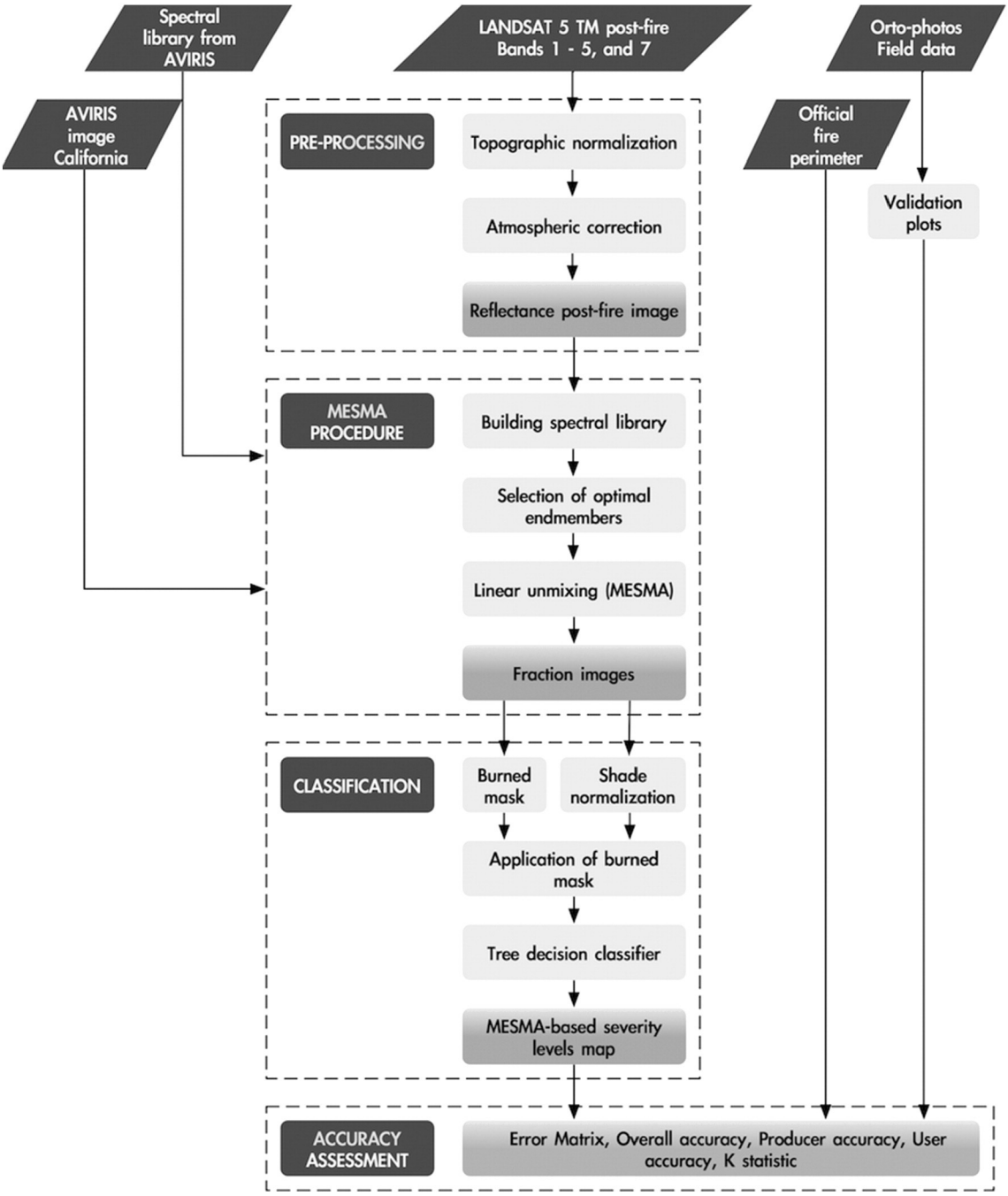


**Fig. 2.** Flowchart of methodology.

accuracy assessment. First, TM pre- and post-fire images were pre-processed. Pre-processing of the remotely sensed data included subsetting, topographic normalization and atmospheric correction (Section 3.1). Second, fraction images were calculated. Prior to applying MESMA (Roberts et al., 1998), an extension of simple LSMA, we built a spectral library (Section 3.2.1). Both image and reference endmembers were included in the library as candidate endmembers. After selecting the optimal endmembers and building the definitive spectral library (Section 3.2.2), the fraction images were calculated (Section 3.2.3). Third, from the fraction images, we obtained an image of the potentially burned pixels, classified (Section 3.3) into four classes (Unburned (U), Low (L), Moderate (M), and High severity (H)) using a binary decision tree (Friedl & Brodley, 1997). Finally, the accuracy of the estimates was calculated (Section 3.4). We used a minimum of 50 reference plots per class derived from a 50 cm post-fire digital orthophotograph (from the DLR severity levels estimation in the Tenerife study area).

### 3.1. Pre-processing

After being downloaded, all of the images were co-registered to the digital orthophotos provided by the CNIG (to the DLR estimate in Tenerife study area) and to the official GPS burned area perimeters provided by the respective Spanish Regional Governments. Mis-registration error between TM images and post-fire false-color orthophotos was below 0.25 of a pixel. The co-registered images of the three study areas were topographically normalized using the C-correct approach (Teillet et al., 1982) with the help of the GDEM V2 DEM provided by USGS. Finally, all of the Landsat 5 TM images were converted to apparent surface reflectance. The original digital numbers of reflective TM bands were scaled to radiance values ($L_\lambda$) using the procedure proposed by Chander and Markham (2003). The radiance to surface reflectance ($\rho$) conversion was performed by using the image-based cosine of the solar transmittance (COST) method (Chavez, 1996). Path radiance ($L_p$) values were computed by using the formulae reported in Song et al. (2001) which assumes 1% surface reflectance for dark objects (Chavez, 1989, 1996). The optical thickness for Rayleigh scattering ($\rho_r$) was estimated according to the equation given in Kaufman (1989).

In the Tenerife study, due to the presence of some clouds, we needed to define a 'cloud mask' image. We used an adaptation of the algorithm proposed by Chuvieco and Hantson (2010) that the National Geographic Institute of the Spanish Government adopted to process the medium resolution satellite images in the frame of the Spanish Remote Sensing National Planning. In addition, we defined a 'sea mask' to identify all the 'sea' pixels in the image.

### 3.2. MESMA procedure

MESMA extends LSMA by allowing the number and types of endmembers to vary on a per-pixel basis (Roberts et al., 1998). MESMA overcomes limitations of LSMA by requiring a model to meet minimum fit, fraction and residual constraints while testing multiple models for each image pixel. Using this approach, significantly more than four materials can be mapped across an image, while minimizing pixel-scale fraction errors by selecting the best-fit model for each pixel. Typical endmembers used in MESMA include soil, green vegetation (GV), non-photosynthetic vegetation (NPV) and shade. The MESMA procedure presented here consists of three steps: 1) building a spectral library. Both image and reference endmembers were included in the library as candidate endmembers; 2) selection of the optimal endmembers to form the definitive spectral library; and 3) decomposing the mixed pixels to calculate the fraction images.

#### 3.2.1. Building the spectral library

Two alternatives exist to define endmember spectra (Settle & Campbell, 1998). The first one uses reflectance values extracted from spectral libraries (reference endmember). Reference endmembers can be derived from the field, laboratory, images or even radiative transfer models. The second option utilizes spectra derived from the image (image endmembers). According to Drake et al. (1999), reference endmembers have the advantage of being pure and, therefore, fractions obtained will be absolute. Their disadvantages are that image correction is not trivial and errors are always introduced. On the other hand, image endmembers presents two advantages: 1) they are easily obtained and 2) they have the same scale of measurement as the data.

We used both types of endmembers to form the spectral library with the candidate endmembers. On one hand, we extracted some endmembers from the spectral library based on AVIRIS data of California area, and from the AVIRIS image. Specifically, the post-fire AVIRIS image provided non-photosynthetic vegetation and ash spectra, and the AVIRIS-based spectral library, provided mainly spectra from vegetation canopies (shrub, herb) and from impervious surfaces. On the other hand, we also used endmembers extracted from the TM imagery, mainly ash and vegetation canopies spectra. In this case, we selected the endmember spectra based on three criteria: the Purity Pixel Index (PPI), our knowledge of the study areas, and the general spectral shape of the considered spectra. We first applied a minimum noise fraction (MNF) transformation and the PPI algorithm. The MNF (essentially two cascaded principal components transformations) was used to determine the inherent dimensionality of image data, to segregate noise in the data, and to reduce the computational requirements for subsequent processing (Boardman & Kruse, 1994). The new MNF transformed bands were then analyzed to find the most spectrally pure (extreme) pixels in the image using PPI. The PPI image was the result of several thousand iterations of the PPI algorithm. The higher values indicated pixels that are relatively purer than pixels with lower values (Environment for Visualizing Images, ENVI, 2009). Once the purest pixels were identified, we selected visually from them the spectral response of different endmembers by using local knowledge and taking into account the general spectral shape of the considered spectra.

#### 3.2.2. Selection of optimal endmembers

Identifying a high quality set of reference or image endmembers has been defined as a critical stage of mixture modeling (Tompkins et al., 1997). A number of approaches have been developed for identifying those spectra that are most representative of a specific class, yet also least likely to be confused with spectra from a different class. In our work, we used the following three techniques to select the most appropriate endmembers from the set of candidate endmembers: 1) Count-based Endmember Selection (CoB): endmembers are selected that model the greatest number of endmembers within their class (Roberts et al., 2003). As a variation on this approach, a Count-based Index can be used to rank endmember selection based on maximizing the models selected within the correct class, while minimizing confusion with other classes; 2) Endmember Average RMSE (root mean squared error) (EAR): endmembers are selected that produce the lowest RMSE within a class (Dennison & Roberts, 2003); and 3) Minimum Average Spectral Angle (MASA): endmembers are selected that have the lowest average spectral angle (Dennison et al., 2004). All of these approaches together with the MESMA algorithm are available in Visualization and Image Processing for Environmental Research (VIPER) tools software (Roberts et al., 2007) that was used in this work.

CoB determines the number of spectra modeled by an endmember within the endmember's class (InCoB) and outside of the endmember's class (OutCoB). It can be used to rank endmember selection based on maximizing the models selected within the correct class, while minimizing confusion with other classes. CoB uses the MESMA concept to select endmembers based on the number of library spectra each endmember models. The optimum model would have the highest InCoB and lowest OutCoB (Roberts et al., 2003).

EAR can be expressed as Eq. (1) shows:

$$EAR_i = \frac{\sum_{j=1}^{N} RMSE_{i,j}}{n-1} \quad (1)$$

where i is an endmember, j is the modeled spectrum, N is the number of endmembers, and n is the number of modeled spectra. The "−1" corrects for the zero error resulting from an endmember modeling itself. As EAR is based on RMSE from a linear spectral mixing model, it is influenced by albedo. A minimum (0%) and maximum (100%) shade-fraction constraints was applied to decrease the likelihood that very light or very dark spectra would be identified as highly representative endmembers for their class by increasing the RMSE of spectra that exceeded the shade fraction thresholds (Dennison & Roberts, 2003). Finally, MASA is similar to EAR, but uses a spectral angle (θ) as the error metric (Eq. 2).

$$MASA_i = \frac{\sum_{j=1}^{N} \theta_{i,j}}{n-1}. \quad (2)$$

The spectral angle is calculated as displayed in Eq. (3) where $\rho_\lambda$ is the reflectance of an endmember, $\rho'_\lambda$ is the reflectance of a modeled spectrum, $L_\rho$ is the length of the endmember vector and $L_{\rho'}$ is the length of the modeled spectrum vector. The length is calculated as the square root of the sum of reflectance in each wavelength included in the model (Youngentob et al., 2011).

$$\theta = cos^{-1}\left(\frac{\sum_{\lambda=1}^{M} \rho_\lambda \rho_\lambda'}{L_\rho L_{\rho'}}\right). \quad (3)$$

*3.2.3. Unmixing*

Once the most appropriate endmembers were identified by using the above-mentioned measures, they were grouped into three different spectral libraries. Our approach is based on assumption that every pixel in original images can be modeled by a linear combination of three land-cover types: NPV or ash, GV and soil. Shade is typically also present in all pixels. Trials using just one or two spectral libraries showed that three libraries (four endmembers) were needed to model accurately the Landsat 5 TM images.

Thus, the original image was unmixed into those four endmembers (NPV or ash, GV, soil, and shade) using MESMA. Performance of all models for each pixel was evaluated by selecting the model with the lowest RMSE, with the condition that the RMSE of the best-fit model may not exceed some user-defined threshold. For the best-fit model for each pixel, the fraction values for each endmember, and the identity of those endmembers were recorded. Criteria used to evaluate models using MESMA include fractions, maximum shade fraction and RMSE. Similar to Roberts et al. (2003), Powell et al. (2007) and Roberts et al. (2012), we used the following selection criteria: minimum and maximum allowable fraction values, −0.05 and 1.05, respectively; maximum allowable shade fraction value, 0.8; and maximum allowable RMSE, 0.025. When multiple models met these criteria, the model with the lowest RMSE was selected.

By varying the set the spectra considered in each spectral library each time, we could obtain different sets of fraction images. The more adequate set of fraction images was selected visually in a first stage, and secondly, by classifying the fraction images and computing the accuracy of the severity level estimate. Therefore, the selection of the number and type of spectra included in each spectral library as well as the unmixing of the image, were remade until the fraction images obtained allowed an accurate estimate. In some cases, when the percentage of classified pixels was too low, the building of the spectral library needed to be refined as well by introducing a new type of spectra that characterizes the unclassified areas.

*3.3. Classification*

Our classification stage included three steps. First, we constructed an image of potential burned pixels from the fraction images (we called 'burned mask'). To do that, we selected the pixels that simultaneously met three conditions: 1) their NPV–Ash fraction was higher than the average of the image; 2) their GV fraction was lower than the average; and 3) their model included an "ash" endmember. Second, we performed a shade normalization of the fraction images obtained by dividing each endmember by the total percent cover of all non-shade endmembers (1-shade fraction) in each pixel. This suppresses the shade fraction so that we obtain more information on the relative abundance of non-shade endmembers (Rogan & Franklin, 2001). Third, the 'burned mask' was applied to the shade normalized fraction images (i.e. NPV–Ash, GV, soil).

Finally, an estimation of severity levels (U, L, M and H) was achieved by classifying the masked shade normalized fraction images. A decision tree was used as the classifier. Decision trees are rule-based classifiers that employ a top-down induction approach to input data and recursively partition data feature spaces into increasingly homogenous classes based on a splitting criterion (Franklin, 1998; Friedl et al., 1999). The efficiency of tree-classifiers, when compared to commonly used classifiers such as maximum likelihood, has been attributed to their non-parametric nature, in that they do not require assumptions regarding the distributions of the input data (Friedl & Brodley, 1997). We used the decision tree implemented in the R software (Ripley, 1996). The tree was grown by binary recursive partitioning. Numeric variables are divided into 'X < a' and 'X > a', and the split which maximizes the reduction in impurity is chosen; the data set split and the process repeated. Splitting continues until the terminal nodes are too small or too few to be split (Breiman et al., 1984). A minimum of 20 pixels per class was selected to train the tree.

*3.4. Accuracy assessment*

Following Congalton and Green (2009), our study used the κ statistic to measure the accuracy of the achieved severity level estimate. Overall accuracy (OA), producer's accuracy (PA) (omission error) and user's accuracy (UA) (commission error) for each class were calculated as well. As ground reference, we used a minimum of 50 validation plots per class defined from a 50 cm post-fire orthophoto inside the fire perimeter. We defined the validation plots considering three burn severity levels: high severity, moderate severity and low severity, and the unburned class as well. Our sample unit is a plot of 50 × 50 m. Classification of each plot was determined by visual inspection, based on the observed majority burn severity class within each plot (Fig. 3). Areas where the proportion of dead tree was over 90% (top dead) were classified as H class (High severity level). Areas where the proportion of dead tree was between 50 and 90% (top dead) were classified as M class (Moderate severity level), and areas where the proportion of dead tree was below 50%, giving a mosaic state between living and dead individuals, were classified as L class (Low severity level). Additionally, we randomly sampled the surface outside the fire perimeter (U class, Unburned), considering approximately the same percentage of pixels as the percentage of pixels included in the validation plots inside the perimeter.

Following Congalton and Green (2009) we utilized a minimum of 50 plots for each class of interest inside of the fire perimeter (that is, finally we considered a little more than the 1% of the pixels inside the fire perimeter). We also used a random scheme to select the 1% of the pixels outside of the fire perimeters (U class, Unburned). It should be noted that the results could be biased towards the use of satellite data because our reference truth is based on canopy observations taken at greater spatial resolution than the Landsat data, and our visual interpretation, on the other hand, may be subjective.

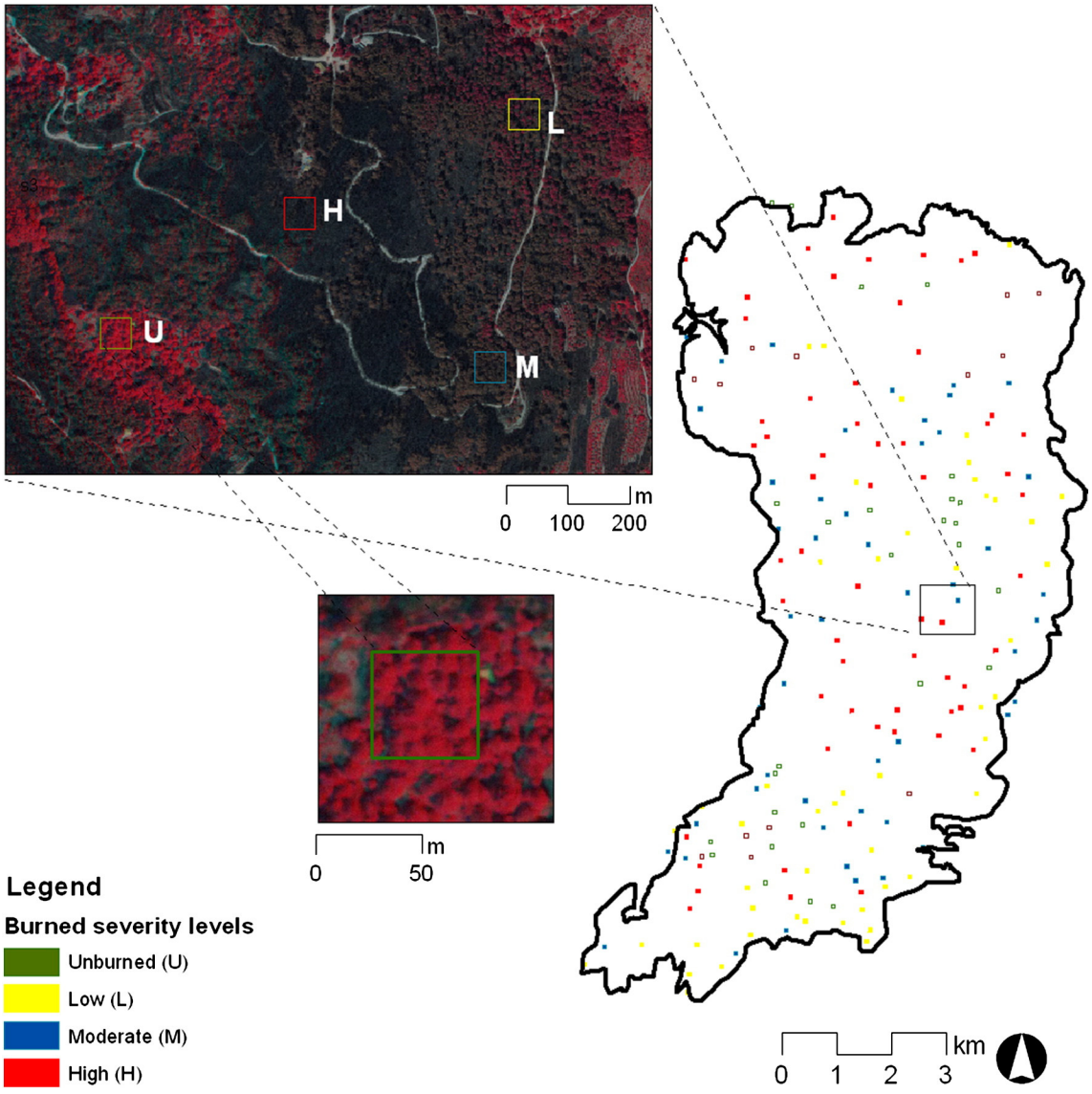


**Fig. 3.** Example of validation plots (Ávila study area).

## 4. Results

### 4.1. MESMA procedure

As indicated in Methods section, we built our spectral libraries using spectra from three sources. From the AVIRIS image we extracted spectra of two endmembers: ash and NPV. We also selected spectra from the AVIRIS spectral library; specifically we chose spectra for the following endmembers: non-photosynthetic herb, green herb, green shrub, and impervious surfaces. All of the endmembers selected from AVIRIS data were re-sampled to TM wavelengths before using them. We complemented AVIRIS spectra with image endmembers from some of the purest pixels from the Landsat 5 TM images. Image endmembers included ash, un-irrigated lands, irrigated crops, vegetation species and soils representative of each study area. Regarding vegetation species, we used: *P. pinaster*, and *Quercus* sp., in the Guadalajara study area; *P. pinaster*, *P. sylvestris*, *Q. pyrenaica*, and *Q. ilex* in the Ávila study area; and, in the Tenerife study area, *P. canariensis*, *E. arborea*, and *M. faya*. As regards soils, the Tenerife study area displayed a higher variety: we defined till four different types of basaltic rocks.

After computing for CoB, EAR and MASA, we selected the endmember signatures with the highest CoB, and also the lowest EAR and the lowest MASA. Working in this way, we could reduce the number of spectra that form the final and definitive spectral library. The selected spectra were grouped into different spectral libraries to allow us to unmix various combinations of two, three and four endmembers. In the three study areas, the combination that leads to the highest accurate burn severity estimation was to use three spectral libraries: NPV–Ash, GV and soil. Typically, and as Table 2 shows, the NPV–Ash library included the following types of endmembers: NPV and ash from the AVIRIS image, non-photosynthetic herb from the AVIRIS-based spectral library, and ash and un-irrigated lands from the Landsat 5 TM image. The GV library comprised: green herb and green shrub from the AVIRIS-based spectral library, and irrigated crops and vegetation representative of each study area from the Landsat 5 TM images. Finally, the soil library included: impervious surfaces (asphalt and gray gravel roof) from the AVIRIS spectral library, and soils representative of each study area from the Landsat 5 TM images. To summarize, the reference endmembers provided information general or common to all study areas, whereas the image endmembers mainly provided information specific to each study area. Despite the similarity between Californian and Mediterranean vegetation, we needed to include in each study area its specific vegetation species and soil types. Thus, green vegetation endmembers were mainly defined from each Landsat

**Table 2**
Spectral libraries and endmembers used in the MESMA procedure.

| Spectral library | Endmember | Endmember type | Number of endmembers | | |
|---|---|---|---|---|---|
| | | | Guadalajara | Ávila | Tenerife |
| NPV and Ash | NPV | Reference (APFI) | 3 | – | 1 |
| | NP herb | Reference (ASL) | 1 | – | 1 |
| | Ash | Reference (APFI) | – | – | 2 |
| | Ash | Image | 9 | 4 | – |
| | Un-irrigated lands | Image | – | 2 | – |
| | Total | | 13 | 6 | 4 |
| GV | Green herb | Reference (ASL) | 1 | 1 | – |
| | Green shrub | Reference (ASL) | 1 | 1 | – |
| | Irrigated crops | Image | 1 | 2 | 1 |
| | Vegetation species[a] | Image | 2 | 7 | 4 |
| | Total | | 5 | 11 | 5 |
| Soil | Impervious surfaces | Reference (ASL) | – | – | 1 |
| | Soils[a] | Image | 4 | 5 | 4 |
| | Total | | 4 | 5 | 5 |

Note: NPV: non-photosynthetic vegetation; NP: non-photosynthetic; GV: green vegetation; APFI: AVIRIS post-fire image; ASL: AVIRIS-based spectral library.
[a] Vegetation species/soils representative of each study area.

5 TM image. As an example, Fig. 4 shows some of the spectra of each spectral library used to unmix the Ávila study area post-fire image, letting us to compare the spectra of the three different sources.

Using the definitive spectral libraries, 99.5%, 99.8% and 98.7%, of the pixels met the 0.025 RMSE criterion at Guadalajara, Avila and Tenerife, respectively. It is remarkable that these values represent almost the 100% of the images. Fig. 5 shows the set of fraction images finally obtained in the Ávila study area. It is possible to observe visually that both NPV–Ash and GV fraction images clearly identify the burned area. The image reporting model number (the specific combination of spectra used in each pixel to unmix the image) also clearly shows the burned area.

### 4.2. Classification

Using the previously mentioned NPV–Ash and GV fraction images and the number of model image, we defined a 'burned mask' that groups all the potential burned pixels (regardless their severity level). Before applying the mask to the fraction images, they were shade normalized. We decided that the best option is to permit a high commission error in this mask, assuring that all the burned pixels were selected. The next classification step (decision tree classifier) deals with the task of reducing such error.

Due to the existence of unburned pixels in the masked shade normalized fraction images (commission error), we considered more than the four classes of interest (H, M, L, and U) to classify them. All of the study areas shared 4 classes: H, M, L, and 'Empty' (pixels that were not selected by the 'burned mask'). In addition, we defined GV, 'soil' and 'reservoir' classes in the Guadalajara study area, GV class in the Ávila study area, and 'ria' (inflow of sea water into a river) and two types of 'volcanic lava' classes in the Tenerife study area. A minimum of 20 pixels per class of interest were selected to train the decision tree classifier. After the classification process, the unburned classes ('Empty', GV, 'soil', etc.) were re-combined into the U class and a median $3 \times 3$ filter was applied to the whole image to reduce the 'salt and pepper' noise. The MESMA-based estimates of the burn severity levels obtained can be seen in Fig. 6. Table 3 displays the performance of the decision trees. The residual mean deviance was below 0.3 in the three study areas, and the accuracy of classifications (based only on training data) was always higher than 90% (from 92.2 to 97.5).

### 4.3. Accuracy assessment

To assess the accuracy of burn severity level estimates, we computed for κ statistic, OA, PA and UA. Over 50 validation plots per considered class were defined from a 50 cm post-fire orthophoto inside of fire perimeter (Table 4). For instance, in the Ávila study area, this implied that 566 pixels of a total of 46,485 pixels were inside the perimeter (1.21%) (see Fig. 3). We also selected randomly 1% of the pixels outside the fire perimeter as reference data (7839 pixels).

Table 5 shows the accuracies of MESMA-based burn severity levels estimates. Fraction images produced severity level estimates with high accuracy (κ statistic > 0.78) and quite balanced PA and UA, showing moderate UA values in L and M classes. PA and UA of the H class have values relatively high in Ávila and Guadalajara study areas. Tenerife study area displayed, however, PA and UA values in the H class lower than in the other two study areas, though more than acceptable.

## 5. Discussion

Although there are no studies that use MESMA-based fraction images to estimate burn severity levels, SMA (usually implementing at least the green vegetation and char endmembers) has proven to be efficient in detecting a charcoal signal. Unmixing is therefore advantageous versus other methods because of its strong capability to distinguish between burn and other sparsely vegetated areas (Rogan & Franklin, 2001). Overall, our results complement the findings of a small number of previous studies (e.g. Fernández-Manso et al., 2009; Landmann, 2003; Rogan & Franklin, 2001; Smith et al., 2007a; Sunderman & Weisberg, 2011) that support the use of SMA in mapping burn severity due to its ability to produce fractions representative of sub-pixel

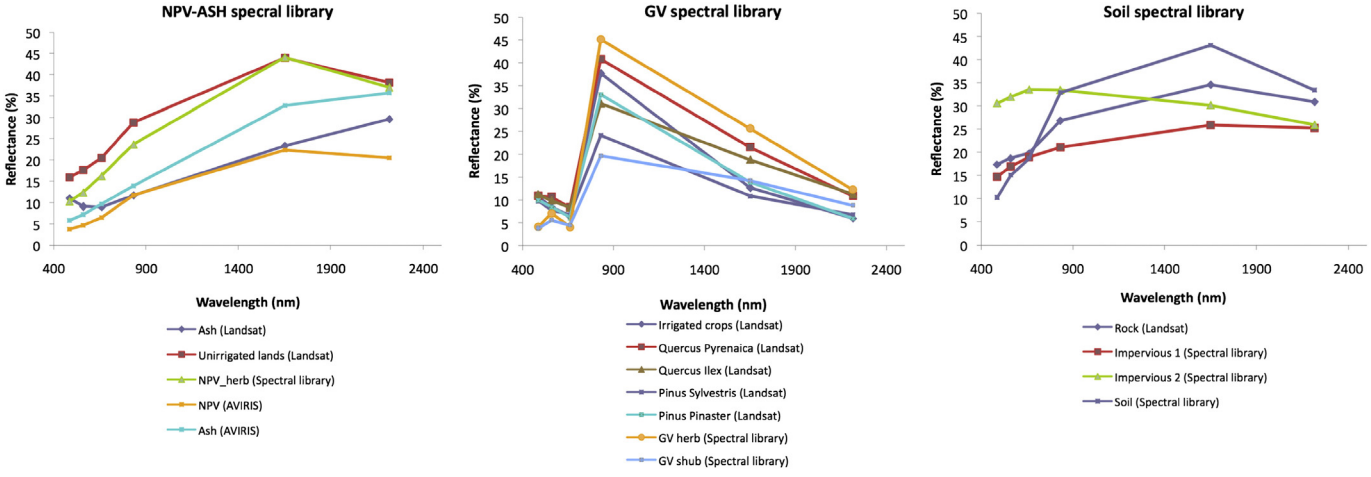


**Fig. 4.** Example spectra from the spectral libraries used in Ávila study area.

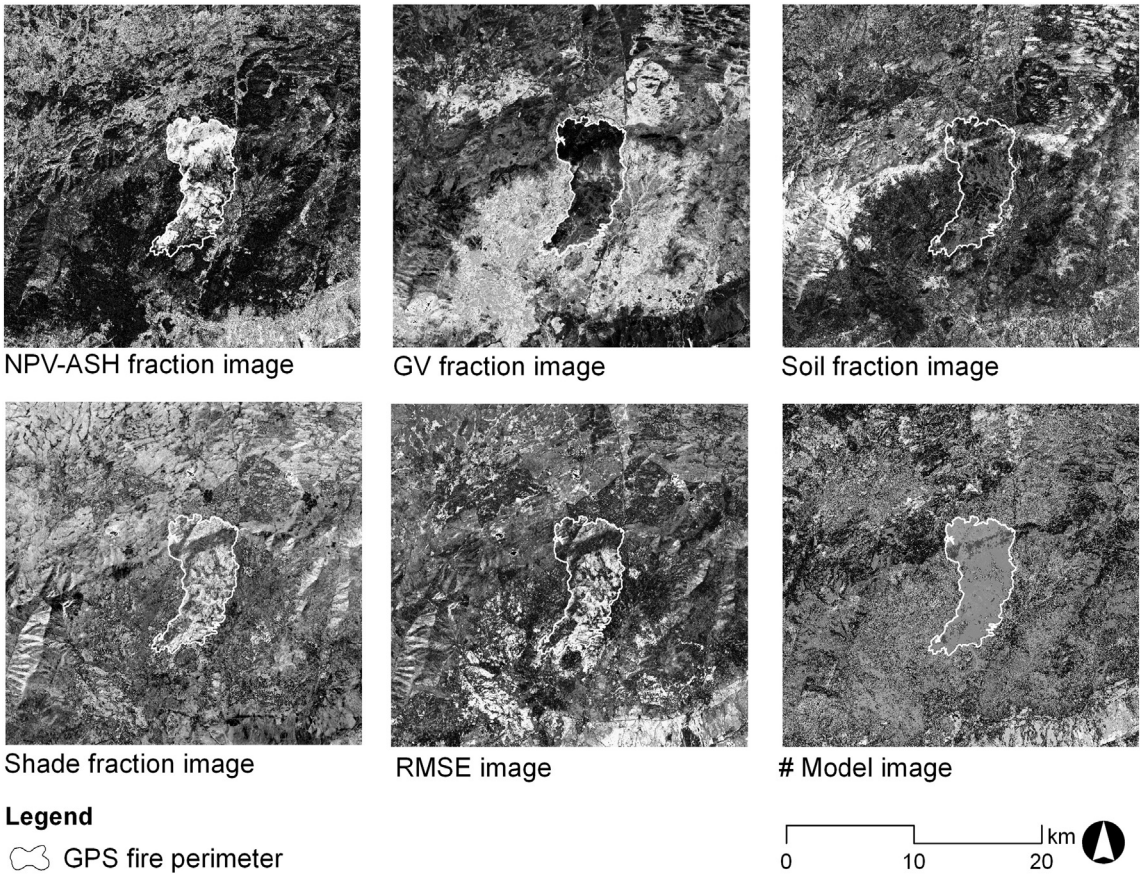


**Fig. 5.** Fraction images (Ávila study area).

components directly related to burn severity. Our study shows that MESMA may be used to derive fraction images from which estimate accurately burn severity, extending the applicability of MESMA.

To provide a better understanding of the MESMA performance in burn severity estimation, Fig. 7 displays the fraction image average inside each class of the estimated severity level (Ávila study area). From this figure, we can follow the differences in the values of fraction images for each class. Compared to all burn classes, U class is characterized by low values in NPV–Ash fraction (meaning low NPV content, and no ashes), medium values in soil fraction and the highest values in GV fraction. L class shows a low value in the NPV–Ash fraction (meaning no NPV, and small quantity of ash), a medium value in soil fraction and a high value in GV fraction. M class displays an increase in the NPV–Ash fraction due to the increase of ash, and a decrease in soil and green vegetation to compensate the increase in ash. Finally, H class continues with the tendency of M class: an increase in the NPV–Ash fraction and a decrease in soil and GV fractions.

Additionally, from Fig. 7 it is possible to observe some differences among the three considered fires. We observed in the three study areas how the proportion of NPV–Ash increased from U class to H class and the proportion of GV decreased. The soil proportion displayed a more irregular pattern among the considered study areas, due probably to differences in vegetation and soil type, and fire evolution. The differences are more evident in Tenerife study area where the proportion of soil are high for all burn classes. The reason is that, as mentioned in Section 2, the study area is located over a volcanic surface where vegetation is sparse, especially in high elevation areas.

However, we would like to note that a careful selection of endmembers plays an important role in the MESMA approach. The determination of endmembers is a critical step to estimating fractional covers accurately. General criteria for a good set of endmembers include linear independency, spectral representativity and spatial generality (Maselli, 1998). High correlation between spectra of endmembers produces an ill-conditioned model and estimates from the decomposition are unreliable, while the use of non-representative endmembers yields large errors in estimates of endmember fractions (Li et al., 2005). A method commonly used in SMA-based studies is the combination of MNF transformation and PPI index (Bedini et al., 2009; Fernández-Manso et al., 2009; Li et al., 2005; Rosso et al., 2005). By contrast, we used three indexes to select the most appropriate endmembers to build the definitive spectral libraries: CoB (Roberts et al., 2003), EAR (Dennison & Roberts, 2003) and MASA (Dennison et al., 2004). In addition, three sources provided us the candidate endmembers: a post-fire 2009 AVIRIS image, a pre-fire 2007 AVIRIS image, and Landsat 5 TM images. The use of reference endmembers from California, also a Mediterranean ecosystem, complemented the set of image endmembers from the Landsat 5 TM data. This procedure leaded to an optimal selection of endmembers, and thus, from the fraction images we could calculate an accurate burn severity estimate.

We acknowledge that the method, as proposed in the present paper, would be applied routinely in an operational scenario with difficulty. Although we provided a single method to build the spectral libraries (combining reference and image endmembers from two Mediterranean ecosystems) and an objective method to select the most appropriate endmembers, we recognize that the unmixing and later classification processes need some supervision. To simplify the building of the spectral libraries, we will consider in a future work the use of the same potential spectral library to all forest fires, although we accept that non-species-specific spectral curves may not provide an optimal unmixing result (Lentille et al., 2009). Different authors have remarked that spectra of senesced vegetation, green vegetation and char are broadly similar across a wide range of environments

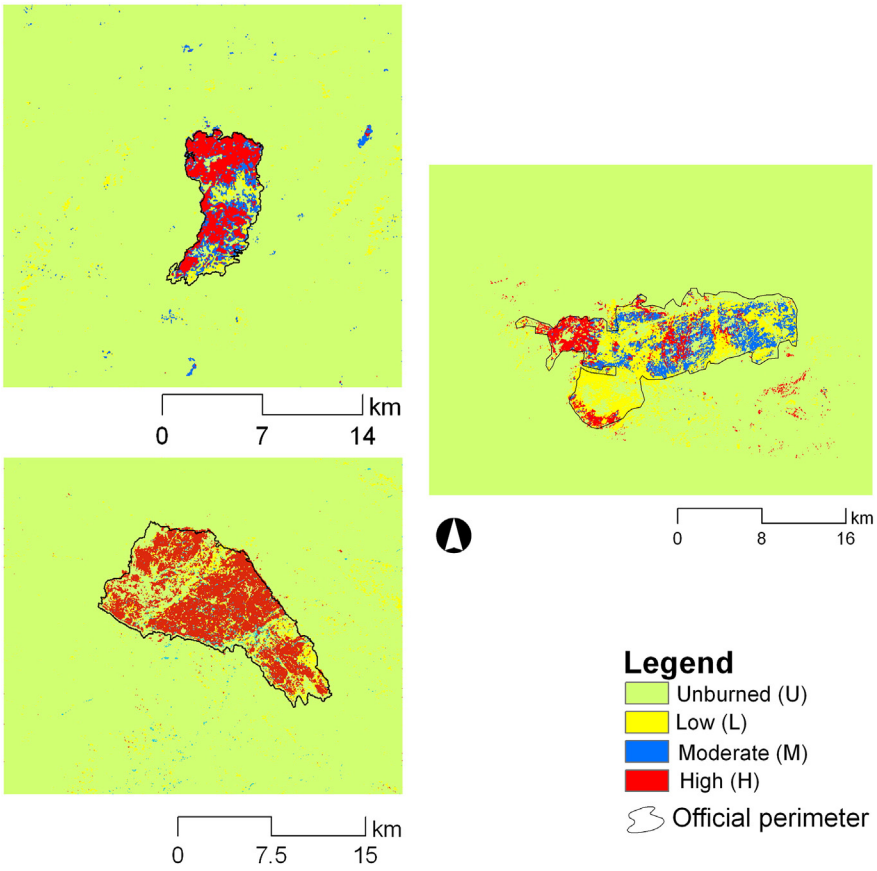


**Fig. 6.** MESMA-based burn severity estimates, top-left: Ávila study area, down-left: Guadalajara study area, right: Tenerife study area.

(Lentille et al., 2009; remote sensing for prediction of 1-year post-fire; Hudak et al., 2007; Smith et al., 2007a). However, in spite of the disadvantage of needing some supervision in the unmixing process, LSMA presents a great advantage over the spectral indexes used commonly to estimate burn severity: fractions images have a physical meaning, thus they are easy to relate to traditional field measurements of burn severity (easy of measure as well).

Simple LSMA, in which a single suite of endmembers are applied to the entire image, limits the number of endmembers to N + 1 bands, although spectral dimensionality is often even lower than this (Roberts et al., 1993). By contrast, MESMA allows a greater number of endmembers, often exceeding the number of bands (e.g. Powell et al., 2007), while also allowing the number and type of endmembers to vary for each pixel within an image (Myint & Okin, 2009; Roberts et al., 1998). In this study, the ability to incorporate a larger number of endmembers to calculate fraction images and map burn severity was critical. First, this enabled us to incorporate five endmembers into the analysis, modeling each pixel as a combination of GV, soil and shade and either NPV or ash. By incorporating NPV into the analysis, this improved the discrimination of burned areas by reducing the confusion caused by bright soils (i.e., burned trunks and branches could add valuable information). Furthermore, this enabled us to account for spectral variability within an endmember class. For example, at the Guadalajara study area the NPV–Ash component required 13 different spectra. Specifically, we used between 4 and 13 in the NPV–Ash spectral library, between 5 and 11 in the GV spectral library, and between 4 and 5 in the soil spectral library between the three study sites (see Table 2).

Some of the forest fires considered in this paper have also been studied by others. De Santis and Chuvieco (2007) compared simulation model inversion and empirical fitting to estimate burn severity levels in Guadalajara study area. They observed that the model inversion was more accurate than the empirical approach when high severity level was considered. Considering The Guadalajara forest fire as well, the same authors (De Santis & Chuvieco, 2009) proposed GeoCBI as an alternative to CBI in Mediterranean countries that takes into account the vegetation fraction cover (FCOV) to compute burn severity of the total plot. de Santis et al. (2009) proposed an improved simulation model to estimate burn severity from satellite data that was also tested in the mentioned study area. Model inversion results showed accurate estimations of GeoCBI values. Comparison among our MESMA-based severity level estimates and the severity level estimates obtained by the De Santis and Chuvieco (2007), or de Santis et al. (2009) at the Guadalajara study area is difficult because we lack quantitative

**Table 3**
Decision tree classifier results.

| Study areas | Guadalajara | Ávila | Tenerife |
|---|---|---|---|
| Number of terminal nodes | 12 | 7 | 8 |
| Misclassification rate | 0.0567 | 0.0781 | 0.0248 |
| Residual mean deviance | 0.3079 | 0.3138 | 0.1389 |
| Accuracy (based on training data) | 94.3 | 92.2 | 97.5 |

**Table 4**
Number of validation plots (and corresponding pixels) defined inside the fire perimeter.

| Class | Guadalajara | | Ávila | | Tenerife | |
|---|---|---|---|---|---|---|
| | V. plots | V. pixels | V. plots | V. pixels | V. plots | V. pixels |
| U | 45 | 180 | 40 | 111 | 43 | 132 |
| L | 79 | 316 | 49 | 133 | 105 | 325 |
| M | 57 | 228 | 51 | 146 | 67 | 216 |
| H | 107 | 428 | 60 | 176 | 86 | 280 |

Note: U: Unburned class, L: Low severity level class, M: Moderate severity level class, H: High severity level; V. plots: Number of validation plots; V. pixels: Number of validation pixels.

**Table 5**
Producer accuracy (PA) (percent) and User accuracy (UA) (percent) per class of burn severity level, Overall accuracy (OA) (percent), and κ statistic of burn severity level estimates.

| | Guadalajara | | | | Ávila | | | | Tenerife | | | |
|---|---|---|---|---|---|---|---|---|---|---|---|---|
| | U | L | M | H | U | L | M | H | U | L | M | H |
| PA | 98.16 | 81.01 | 67.98 | 79.21 | 98.26 | 83.46 | 83.56 | 96.02 | 96.96 | 83.38 | 75.93 | 69.64 |
| UA | 98.88 | 61.84 | 74.88 | 82.48 | 99.77 | 50.45 | 69.71 | 93.89 | 98.68 | 67.58 | 66.67 | 76.47 |
| OA | 95.94 | | | | 97.73 | | | | 93.91 | | | |
| κ | 0.80 | | | | 0.81 | | | | 0.78 | | | |

Note: U: Unburned class, L: Low severity level class, M: Moderate severity level class, H: High severity level class.

information. Visual comparison of the final severity level map (Fig. 7, De Santis & Chuvieco, 2007; Fig. 8, De Santis et al., 2009) allows us to affirm that the results are similar in general terms. As de Santis et al. (2009) affirmed, all burn severity maps show three high severity areas that represent the majority of pixels, separated by two NE–SW diagonal belts with lower values. Main differences arise in these lower values: our MESMA-based estimate suggests that the lower values are mainly unburned areas or areas affected with low severity. By contrast, these areas are classified as medium–low burn severity by De Santis.

After classifying the normalized fraction images, we applied a 3 × 3 median filter to reduce high frequency variations ('salt and pepper' noise) and portray only the burn severity levels. This filtering is a common post-classification procedure to remove outliers or impulse-like noises (Gao, 2009; Mather, 2004) that helps to increase the accuracy of classified image. We did not evaluate how the smoothing (of all image, only of areas inside the burned perimeter, or only of areas outside burned perimeter; pre- or post-classification) affected the UA and PA. Several studies (Quintano & Cuesta, 2010; Quintano et al., 2011), however, have shown that a pre-classification filtering of every pixel in the image increases the accuracy of burned area estimates from remote sensed satellite data. PA and UA values for each burn severity class were quite balanced in all study areas, with the exception of L class, that showed lower UA values than PA values. This higher commission error for L class could correspond with a slightly higher omission error for M class in Guadalajara study area, suggesting some confusion between L and M classes.

Severely burned areas are a focus for land managers after wildfire. Minimizing classification errors for the high severity class will prove beneficial to land managers since it allows identification of more areas that are severely burned (Miller & Thode, 2007). In this study, MESMA-based burn estimates resulted in high PA and UA values for each burn severity class in all study areas, especially for H class. Tenerife study area had lower PA and UA values in this class due probably to the terrain complexity that increased the difficulty to model it correctly. It is a mountainous area with different volcanic soils.

There is no single consistent method that can be applied to assess burn severity via remote sensing, making additional ecosystem-specific studies that relate field-based measures of burn severity to remote sensing observations critical (French et al., 2008; Key, 2005). In Spain, a Mediterranean country, we have validated the proposed MESMA-based method that we believe could be extensible to other Mediterranean ecosystems. Further work with MESMA-based fraction images in a multi-temporal change detection context should provide greater reduction in confusion between the different severity levels. Sunderman and Weisberg (2011) stated that using SMA in a change detection context (dSMA), with multi-temporal imagery, seems promising for reducing this error associated with background conditions in areas that burned repeatedly, because if changes in sub-pixel

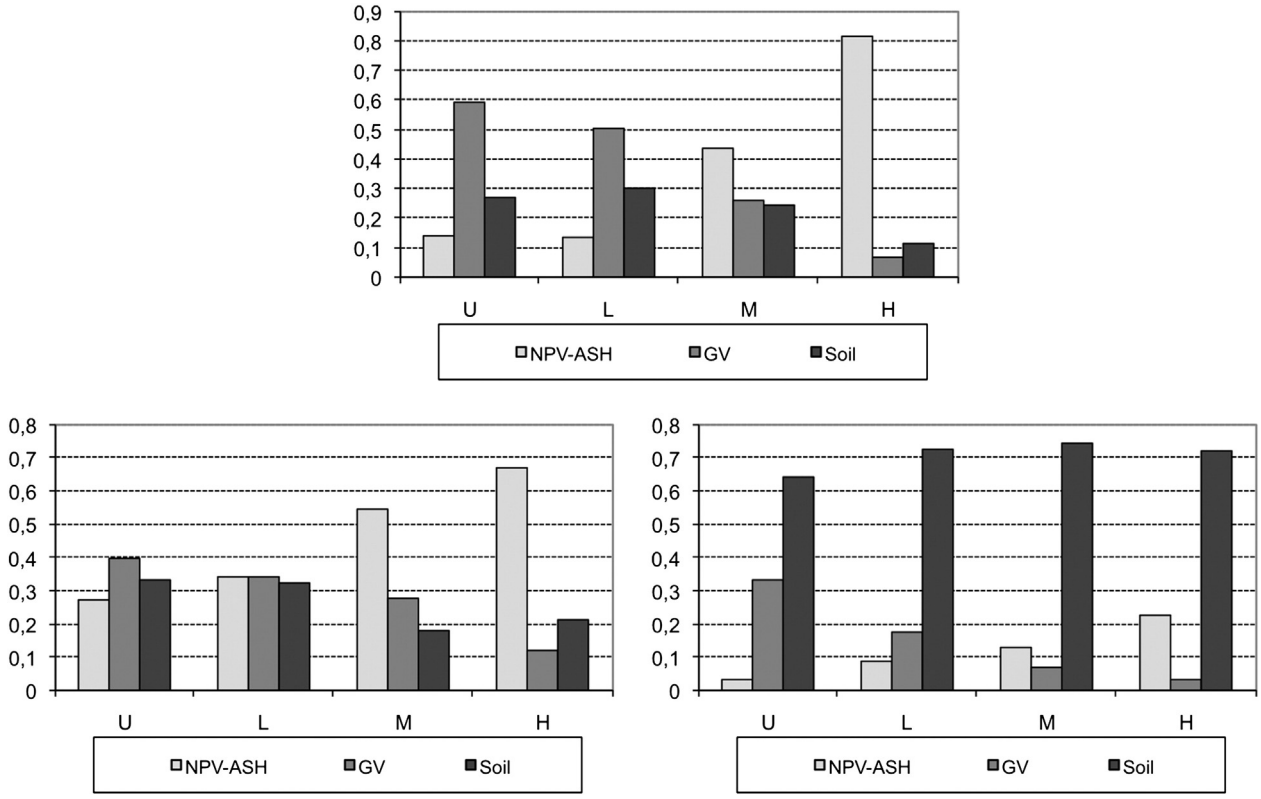


**Fig. 7.** Fraction image average value in each severity level class. Left: Guadalajara study area; center: Ávila study area; right: Tenerife study area.

proportions of the environmental elements that are commonly confused with burned areas can be accounted for, the burned area perimeter should become more spectrally distinguishable. This will be examined in a future work.

## 6. Conclusion

Spectral indexes are commonly used to map post-fire effects. The relationship between these spectral indexes and burn severity in the Mediterranean countries is, however, subject of numerous research studies, showing a lack of a definitive methodology to accurately map burn severity in these countries. In this study, a MESMA-based methodology for burn severity accurately mapping at regional scale in Mediterranean countries from Landsat 5 TM data was validated in three study areas located in Spain. Shade normalized fraction images from MESMA were classified by a decision tree in four classes: unburned, low, moderate and high severity levels. The comparison of the burn severity level estimates in relation to the GPS burned area perimeters and post-fire orthophotographs shows that the methodology adequately maps the severity levels.

The accuracy ($\kappa$ statistic) of the MESMA-based burn severity estimate was high. PA and UA values were quite balanced and high for the high severity level class. However, we would like to acknowledge that a careful selection of endmembers that represent all land covers under study plays an important role in the MESMA-based approach. In our study, the definitive spectral library comprised both image and reference endmembers, and CoB, EAR and MASA allow an optimal selection of definitively used endmembers. A four-endmember model (NPV–Ash, GV, soil and shade) leads to the most accurate burn severity estimates.

We conclude that the MESMA-based proposed method may help to provide a better understanding of severity levels patterns that can be helpful to fire management agencies.

## Acknowledgments

This work was funded in part by Spanish Education Ministry grants (Salvador de Madariaga program) to the two first authors (codes PR2011-0555 and PR2011-0556, respectively) to support a research visit at VIPER Lab. (University of California, Santa Barbara). Equally, all the authors would like to thank the Ministry of Environment of the Castilla y León regional government for its collaboration in this work. Finally, the authors wish to thank two anonymous reviewers who significantly improved the quality of the manuscript.

## References

Adams, J. B., Smith, M. O., & Johnson, P. E. (1993). Imaging spectroscopy: Interpretation based on spectral mixture analysis. In C. M. Pieters, & P. A. J. Englert (Eds.), *Remote geochemical analysis: Elemental and mineralogical composition* (pp. 145–164). Cambridge, England: Cambridge University Press.

Atkinson, P. M., Cutler, M. E. J., & Lewis, H. (1997). Mapping sub-pixel proportional land cover with AVHRR imagery. *International Journal of Remote Sensing*, *18*, 917–935.

Ballantine, J. -A. C., Okin, G. S., Prentiss, D. E., & Roberts, D. A. (2005). Mapping landforms in North Africa using continental scale unmixing of MODIS imagery. *Remote Sensing of Environment*, *97*, 470–483.

Bedini, E., van der Meer, F., & van Ruitenbeek, F. (2009). Use of HyMap imaging spectrometer data to map mineralogy in the Rodalquilar caldera, southeast Spain. *International Journal of Remote Sensing*, *30*, 327–348.

Boardman, J. W., & Kruse, F. A. (1994). Automated spectral analysis: A geologic example using AVIRIS data, north Grapevine Mountains, Nevada. *Proceedings of Tenth Thematic Conference on Geologic Remote Sensing* (pp. I-407–I-418). Ann Arbor, MI: Environmental, Research Institute of Michigan.

Boardman, J. W., Kruse, F. A., & Green, R. O. (1995). Mapping target signatures via partial unmixing of AVIRIS data. *Summaries of the 5th JPL Airborne Earth Science Workshop* (pp. 23–26). Pasadena, California: JPL Publication.

Bodi, M. B., Mataix-Solera, J., Doerr, S. H., & Cerda, A. (2011). The wettability of ash from burned vegetation and its relationship to Mediterranean plant species type, burn severity and total organic carbon content. *Geoderma*, *160*, 599–607.

Breiman, L., Friedman, J. H., Olshen, R. A., & Stone, C. J. (1984). *Classification and regression trees*. Wadsworth.

Calvo, L., Santalla, S., Valbuena, L., Marcos, E., Tárrega, R., & Luis-Calabuig, E. (2008). Post-fire natural regeneration of a *Pinus pinaster* forest in NW Spain. *Plant Ecology*, *197*(1), 81–90.

Chander, G., & Markham, B. (2003). Revised Landsat-5 TM radiometric calibration procedures and postcalibration dynamic ranges. *IEEE Transactions on Geoscience and Remote Sensing*, *41*, 2674–2677.

Chavez, P. S., Jr. (1989). Radiometric calibration of Landsat Thematic Mapper multispectral images. *Photogrammetric Engineering and Remote Sensing*, *55*, 1285–1294.

Chavez, P. S., Jr. (1996). Image-based atmospheric corrections — Revisited and improved. *Photogrammetric Engineering and Remote Sensing*, *62*, 1025–1036.

Chen, X., Vogelmann, J. E., Rollins, M., Ohlen, D., Key, C. H., Yang, L., et al. (2011). Detecting post-fire burn severity and vegetation recovery using multitemporal remote sensing spectral indices and field-collected composite burn index data in a ponderosa pine forest. *International Journal of Remote Sensing*, *32*, 7905–7927.

Chuvieco, E., De Santis, A., Riaño, D., & Halligan, K. (2007). Simulation approaches for burn severity estimation using remotely sensed images. *Journal of Fire Ecology*, *3*, 129–150.

Chuvieco, E., & Hantson, S. (2010). Documento técnico de los algoritmos a aplicar sobre las imágenes de satélite de media resolución [Technical note about the algorithms to use over medium resolution satellite imagery]. *Plan Nacional de Teledetección de Media Resolución Remote Sensing National Planning*. Instituto Geográfico Nacional. Gobierno de España (National Geographic Institute. Government of Spain).

Congalton, R. G., & Green, K. (2009). *Assessing the accuracy of remotely sensed data* Principles and practices (2nd ed.). Boca Raton: CRC Press. Taylor & Francis.

de Santis, A., Asner, G. P., Vaughan, P. J., & Knapp, D. E. (2010). Mapping burn severity and burning efficiency in California using simulation models and Landsat imagery. *Remote Sensing of Environment*, *114*, 1535–1545.

de Santis, A., & Chuvieco, E. (2007). Burn severity estimation from remotely sensed data: Performance of simulation versus empirical models. *Remote Sensing of Environment*, *108*, 422–435.

de Santis, A., & Chuvieco, E. (2009). GeoCBI: A modified version of the Composite Burn Index for the initial assessment of the short-term burn severity from remotely sensed data. *Remote Sensing of Environment*, *113*, 554–562.

de Santis, A., Chuvieco, E., & Vaughan, P. (2009). Short-term assessment of burn severity using the inversion of PROSPECT and GeoSail models. *Remote Sensing of Environment*, *113*, 126–136.

Dennison, P. E., Charoensiri, K., Roberts, D. A., Peterson, S. H., & Green, R. O. (2006). Wildfire temperature and land cover modeling using hyperspectral data. *Remote Sensing of Environment*, *100*, 212–222.

Dennison, P. E., Halligan, K. Q., & Roberts, D. A. (2004). A comparison of error metrics and constraints for Multiple Endmember Spectral Mixture Analysis and Spectral Angle Mapper. *Remote Sensing of Environment*, *93*, 359–367.

Dennison, P. E., & Roberts, D. A. (2003). Endmember selection for mapping chaparral species and fraction using Multiple Endmember Spectral Mixture Analysis. *Remote Sensing of Environment*, *41*, 123–135.

Díaz-Delgado, R., Lloret, F., & Pons, X. (2003). Influence of fire severity on plant regeneration by means of remote sensing imagery. *International Journal of Remote Sensing*, *24*, 1751–1763.

Drake, N. A., Mackin, S., & Settle, J. J. (1999). Mapping vegetation, soils, and geology in semiarid shrublands using spectral matching and mixture modeling of SWIR AVIRIS imagery. *Remote Sensing of Environment*, *68*, 12–25.

Eckmann, T. C., Roberts, D. A., & Still, C. J. (2009). Estimating subpixel fire sizes and temperatures from ASTER using Multiple Endmember Spectral Mixture Analysis. *International Journal of Remote Sensing*, *30*, 5851–5864.

Environment for Visualizing Images (ENVI) Software v. 4.7 (2009). ITT visual information solution. www.ittivis.com

Epting, J., & Verbyla, D. (2005). Landscape-level interactions of prefire vegetation, burn severity, and postfire vegetation over a 16-year period in interior Alaska. *Canadian Journal of Forest Research*, *35*, 1367–1377.

Epting, J., Verbyla, D., & Sorbel, B. (2005). Evaluation of remotely sensed indices for assessing burn severity in interior Alaska using Landsat TM and ETM+. *Remote Sensing of Environment*, *96*, 328–339.

Fernández-Manso, O., Quintano, C., & Fernández-Manso, A. (2009). Combining spectral mixture analysis and object-based classification for fire severity mapping. *Forest Systems*, *18*, 296–313.

Franke, J., Roberts, D. A., Halligan, K., & Menz, G. (2009). Hierarchical Multiple Endmember Spectral Mixture Analysis (MESMA) of hyperspectral imagery for urban environments. *Remote Sensing of Environment*, *113*, 1712–1723.

Franklin, J. (1998). Predicting the distribution of shrub species in Southern California from climate and terrain-derived variables. *Journal of Vegetation Science*, *9*, 733–748.

French, N. H. F., Kasischke, E. S., Hall, R. J., Murphy, K. A., Verbyla, D. L., Hoy, E. E., et al. (2008). Using Landsat data to assess fire and burn severity in the North American Boreal Forest Region: An overview and summary of results. *International Journal of Wildland Fire*, *17*, 443–462.

Friedl, M. A., & Brodley, C. E. (1997). Decision tree classification of landcover from remotely sensed data. *Remote Sensing of Environment*, *61*, 399–408.

Friedl, M. A., Brodley, C. E., & Strahler, A. H. (1999). Maximizing landcover classification accuracies produced by decision trees at continental to global scales. *IEEE Transactions on Geoscience and Remote Sensing*, *37*, 969–977.

Gao, J. (2009). *Digital analysis of remotely sensed imagery*. McGraw-Hill Companies Inc. (698 pp.).

Herold, M., Roberts, D. A., Gardner, M. E., & Dennison, P. E. (2004). Spectrometry for urban area remote sensing — Development and analysis of a spectral library from 350 to 2400 nm. *Remote Sensing of Environment*, *91*, 304–319.

Hudak, A., Morgan, P., Bobbitt, M., Smith, A., Lewis, S., Lentile, L., et al. (2007). The relationship of multispectral satellite imagery to immediate fire effects. *Journal of Fire Ecology*, *3*, 64–90.

Hudak, A., Morgan, P., Stone, C., Robichaud, P., Jain, T., & Clark, J. (2004). The relationship of field burn severity measures to satellite-derived Burned Area Reflectance Classification (BARC) maps. *American Society for Photogrammetry and Remote Sensing Annual Conference Proceedings* (pp. 96–104) (CD-ROM).

Jain, T. B., Pilliod, D., & Graham, R. T. (2004). Tongue-tied. Confused meanings for common fire terminology can lead to fuels mismanagement. A new framework is needed to clarify and communicate the concepts. *Wildfire*, *4*, 22–26.

Kaufman, Y. J. (1989). The atmospheric effect on remote sensing and its corrections. In G. Asrar (Ed.), *Theory and applications of optical remote sensing* (pp. 336–428). New York, NY: Wiley-Interscience.

Keeley, J. E. (2009). Fire intensity, fire severity and burn severity: A brief review and suggested usage. *International Journal of Wildland Fire*, *18*, 116–126.

Key, C.H. (2005). Remote sensing sensitivity for fire severity and fire recovery. Pages 29–39 in: J. Riva, F. Pérez-Cabello and E. Chuvieco, editors. Proceedings of the 5th International Workshop on Remote Sensing and GIS applications to Forest Fire Management: Fire Effects Assessment. Universidad de Zaragoza, Spain, and GOFC-GOLD, EARSeL, Paris, France.

Key, C. H., & Benson, N. C. (2006). Landscape assessment (LA). Sampling and analysis methods. *USDA Forest Service Gen. Tech. Rep. RMRS-GTR-164-CD*.

Kokaly, R. F., Rockwell, B. W., Haire, S. L., & King, T. V. V. (2007). Characterization of post-fire surface cover, soils and burn severity at the Cerro Grande Fire, New Mexico, using hyperspectral and multispectral remote sensing. *Remote Sensing of Environment*, *106*, 305–325.

Landmann, T. (2003). Characterizing sub-pixel Landsat ETM+ fire severity experimental fires in the Kruger National Park, South-Africa. *South African Journal of Science*, *99*, 357–360.

Lentile, L., Holden, Z., Smith, A., Falkowski, M., Hudak, A., Morgan, P., et al. (2006). Remote sensing techniques to assess active fire characteristics and post-fire effects. *International Journal of Wildland Fire*, *15*, 319–345.

Lentille, L. B., Smith, A. M. S., Hudak, A. T., Morgan, P., Bobbitt, M. J., Lewis, S. A., et al. (2009). Remote sensing for prediction of 1-year post-fire ecosystem condition. *International Journal of Wildland Fire*, *18*, 594–608.

Li, L., Ustin, S. L., & Lay, M. (2005). Application of Multiple Endmember Spectral Mixture Analysis (MESMA) to AVIRIS imagery for coastal salt marsh mapping: A case study in China Camp, CA, USA. *International Journal of Remote Sensing*, *26*(23), 5193–5207.

López-García, M. J., & Caselles, V. (1991). Mapping burns and natural reforestation using Thematic Mapper data. *Geocarto International*, *1*, 31–37.

Martín, J. L., García, H., Redondo, C. E., García, I., & Carralero, I. (1995). *La Red Canaria de Espacios Naturales Protegidos.* Consejería de Política Territorial, Viceconsejería de Medio Ambiente, Gobierno de Canarias.

Maselli, F. (1998). Multiclass spectral decomposition of remotely sensed scenes by selective pixel unmixing. *IEEE Transactions on Geoscience and Remote Sensing*, *36*, 1809–1820.

Mather, P. M. (2004). *Computer processing of remotely-sensed images. An introduction* (3rd ed.)Chichester: John Wiley & Sons Ltd (350 pp.).

Miller, J. D., & Thode, A. E. (2007). Quantifying burn severity in a heterogeneous landscape with a relative version of the delta Normalized Burn Ratio (dNBR). *Remote Sensing of Environment*, *109*, 66–80.

Miller, J. D., & Yool, S. R. (2002). Mapping forest post-fire canopy consumption in several overstory types using multi-temporal Landsat TM and ETM data. *Remote Sensing of Environment*, *82*, 481–496.

Myint, S. W., & Okin, G. S. (2009). Modelling land-cover types using Multiple Endmember Spectral Mixture Analysis in a desert city. *International Journal of Remote Sensing*, *30*, 2237–2257.

Otto, R., García-del-Rey, E., Gil, P., & Fernández-Palacios, J. M. (2009). The effect of fire severity on first-year seedling establishment in a *Pinus canariensis* forest on Tenerife, Canary Islands. *European Journal of Forest Research*, *129*, 499–508.

Powell, R. L., Roberts, D. A., Dennison, P. E., & Hess, L. L. (2007). Sub-pixel mapping of urban land cover using Multiple Endmember Spectral Mixture Analysis: Manaus, Brazil. *Remote Sensing of Environment*, *106*, 253–267.

Quintano, C., & Cuesta, E. (2010). Improving satellite image classification by using fractional type convolution filtering. *International Journal of Applied Earth Observation and Geoinformation*, *12*, 298–301.

Quintano, C., Fernández-Manso, A., Fernández-Manso, O., & Shimabukuro, Y. (2006). Mapping burned areas in Mediterranean countries using spectral mixture analysis from a uni-temporal perspective. *International Journal of Remote Sensing*, *27*, 645–662.

Quintano, C., Fernández-Manso, A., Stein, A., & Bijker, W. (2011). Estimation of area burned by forest fires in Mediterranean countries: A remote sensing data mining perspective. *Forest Ecology and Management*, *262*, 1597–1607.

Riaño, D., Chuvieco, E., Ustin, S., Zomer, R., Dennison, P., Roberts, D., et al. (2002). Assessment of vegetation regeneration after fire through multitemporal analysis of AVIRIS images in the Santa Monica Mountains. *Remote Sensing of Environment*, *79*, 60–71.

Riaño, D., Moreno-Ruiz, J., Isidoros, D., & Ustin, S. (2007). Global spatial patterns and temporal trends of burned area between 1981 and 2000 using NOAA–NASA Pathfinder. *Global Change Biology*, *13*, 40–50.

Ripley, B. D. (1996). *Pattern recognition and neural networks.* Cambridge: Cambridge University Press (Chapter 7).

Roberts, D. A., Dennison, P. E., Gardner, M., Hetzel, Y., Ustin, S. L., & Lee, C. (2003). Evaluation of the potential of Hyperion for fire danger assessment by comparison to the Airborne Visible/Infrared Imaging Spectrometer. *IEEE Transactions on Geoscience and Remote Sensing*, *41*, 1297–1310.

Roberts, D. A., Gardner, M., Church, R., Ustin, S., Scheer, G., & Green, R. O. (1998). Mapping chaparral in the Santa Monica Mountains using Multiple Endmember Spectral Mixture models. *Remote Sensing of Environment*, *65*, 267–279.

Roberts, D. A., Halligan, K., & Dennison, P. (2007). *VIPER tools user manual. V1.5.*

Roberts, D. A., Quattrochi, D. A., Hulley, G. C., Hook, S. J., & Green, R. O. (2012). Synergies between VSWIR and TIR data for the urban environment: An evaluation of the potential for the Hyperspectral Infrared Imager (HyspIRI) Decadal Survey mission. *Remote Sensing of Environment*, *117*, 83–101.

Roberts, D. A., Smith, M. O., & Adams, J. B. (1993). Green vegetation nonphotosynthetic vegetation and soils in AVIRIS data. *Remote Sensing of Environment*, *44*, 255–269.

Robichaud, P. R. (2005). Measurement of post-fire hillslope erosion to evaluate and model rehabilitation treatment effectiveness and recovery. *International Journal of Wildland Fire*, *14*, 475–485.

Rogan, J., & Franklin, J. (2001). Mapping wildfire burn severity in Southern California forests and shrublands using enhanced Thematic Mapper imagery. *Geocarto International*, *16*, 91–101.

Rosso, P. H., Ustin, S. L., & Hastings, A. (2005). Mapping marshland vegetation of San Francisco Bay, California, using hyperspectral data. *International Journal of Remote Sensing*, *26*, 5169–5191.

Roy, D. P., Boschetti, L., & Trigg, S. N. (2006). Remote sensing of fire severity: Assessing the performance of the Normalized Burn Ratio. *IEEE Transactions on Geoscience and Remote Sensing*, *3*, 112–116.

Schmuck, G., San-Miguel-Ayanz, J., Camia, A., Durrant, T., Santos-de-Oliveira, S., Boca, R., et al. (2010). Forest fires in Europe 2010. *JCR Scientific and Technical Reports*. Joint Research Centre. Institute for Environment and Sustainability Land Management and Natural Hazards Unit (Report No 11. 98 pp.).

Settle, J., & Campbell, N. (1998). On the errors of two estimators of subpixel fractional cover when mixing is linear. *IEEE Transactions on Geoscience and Remote Sensing*, *36*, 163–170.

Shimabukuro, Y. E., & Smith, J. (1991). The least-squares mixing models to generate fraction images derived from remote sensing multispectral data. *IEEE Transactions on Geoscience and Remote Sensing*, *29*, 16–21.

Smith, A. M. S., Drake, N. A., Wooster, M. J., Hudak, A. T., Holden, Z. A., & Gibbons, C. J. (2007a). Production of Landsat ETM+ reference imagery of burned areas within Southern African savannahs: Comparison of methods and application to MODIS. *International Journal of Remote Sensing*, *28*, 2753–2775.

Smith, A. M. S., Lentile, L. B., Hudak, A. T., & Morgan, P. (2007b). Evaluation of linear spectral unmixing and ΔNBR for predicting post-fire recovery in a North American ponderosa pine forest. *International Journal of Remote Sensing*, *28*, 5159–5166.

Song, C., Woodcock, C. E., Seto, K. C., Lenney, M. P., & Macomber, A. S. (2001). Classification and change detection using Landsat TM data: When and how to correct atmospheric effects. *Remote Sensing of Environment*, *75*, 230–244.

Soverel, N. O., Perrakis, D. D. B., & Coops, N. C. (2010). Estimating burn severity from Landsat dNBR and RdNBR indices across western Canada. *Remote Sensing of Environment*, *114*, 1896–1909.

Spanish Environmental Ministry (2005). *Incendios forestales en España. Decenio 1996–2005.* Cento de coordinación de la información nacional sobre incendios. Ministerio de Medio Ambiente.

Sunderman, S. O., & Weisberg, P. J. (2011). Remote sensing approaches for reconstructing fire perimeters and burn severity mosaics in desert spring ecosystems. *Remote Sensing of Environment*, *115*, 2384–2389.

Teillet, P. M., Guindon, B., & Goodenough, D. G. (1982). On the slope-aspect correction of multispectral scanner data. *Canadian Journal of Remote Sensing*, *8*, 84–106.

Theseira, M. A., Thomas, G., & Sannier, C. A. D. (2002). An evaluation of spectral mixture modeling applied to a semi-arid environment. *International Journal of Remote Sensing*, *23*, 687–700.

Tompkins, S., Mustard, J. F., Pieters, C. M., & Forsyth, D. W. (1997). Optimization of endmembers for Spectral Mixture Analysis. *Remote Sensing of Environment*, *59*, 472–489.

van Wagtendonk, J. W., Root, R. R., & Key, C. H. (2004). Comparison of AVIRIS and Landsat ETM+ detection capabilities for burn severity. *Remote Sensing of Environment*, *92*, 397–408.

Veraverbeke, S., Lhermitte, S., Verstraeten, W. W., & Goossens, R. (2010a). The temporal dimension of differenced Normalized Burn Ratio (dNBR) fire/burn severity studies: The case of the large 2007 Peloponnese wildfires in Greece. *Remote Sensing of Environment*, *114*, 2548–2563.

Veraverbeke, S., Lhermitte, S., Verstraeten, W. W., & Goossens, R. (2011). Evaluation of pre/post-fire differenced spectral indices for assessing burn severity in a Mediterranean environment with Landsat Thematic Mapper. *International Journal of Remote Sensing*, *32*(12), 3521–3537.

Veraverbeke, S., Verstraeten, W. W., Lhermitte, S., & Goossens, R. (2010b). Illumination effects on the differenced Normalized Burn Ratio's optimality for assessing fire severity. *International Journal of Applied Earth Observation and Geoinformation*, *12*, 60–70.

Verbyla, D., & Lord, R. (2008). Estimating post-fire organic soil depth in the Alaskan boreal forest using the Normalized Burn Ratio. *International Journal of Remote Sensing*, *29*, 3845–3853.

Vila, G., & Barbosa, P. (2010). Post-fire vegetation regrowth detection in the Deiva Marina region (Liguria-Italy) using Landsat TM and ETM+ data. *Ecological Modelling*, *221*, 75–84.

Youngentob, K. N., Roberts, D. A., Held, A. A., Dennison, P. E., Jia, X., & Lindenmayer, D. B. (2011). Mapping two *Eucalyptus* subgenera using Multiple Endmember Spectral Mixture Analysis and continuum-removed imaging spectrometry data. *Remote Sensing of Environment*, *115*, 1115–1128.